

Multi-Length Scale-Enriched Continuum-Level Material Model for Kevlar®-Fiber-Reinforced Polymer-Matrix Composites

M. Grujicic, B. Pandurangan, J.S. Snipes, C.-F. Yen, and B.A. Cheeseman

(Submitted May 5, 2012; in revised form June 28, 2012; published online August 3, 2012)

Fiber-reinforced polymer matrix composite materials display quite complex deformation and failure behavior under ballistic/blast impact loading conditions. This complexity is generally attributed to a number of factors such as (a) hierarchical/multi-length scale architecture of the material microstructure; (b) nonlinear, rate-dependent and often pressure-sensitive mechanical response; and (c) the interplay of various intrinsic phenomena and processes such as fiber twisting, interfiber friction/sliding, etc. Material models currently employed in the computational engineering analyses of ballistic/blast impact protective structures made of this type of material do not generally include many of the aforementioned aspects of the material dynamic behavior. Consequently, discrepancies are often observed between computational predictions and their experimental counterparts. To address this problem, the results of an extensive set of molecular-level computational analyses regarding the role of various microstructural/morphological defects on the Kevlar® fiber mechanical properties are used to upgrade one of the existing continuum-level material models for fiber-reinforced composites. The results obtained show that the response of the material is significantly affected as a result of the incorporation of microstructural effects both under quasi-static simple mechanical testing condition and under dynamic ballistic-impact conditions.

Keywords ballistics, composites, Kevlar, material models, microstructural defects

1. Introduction

The subject of the present study is high specific-strength and high specific-stiffness polymeric fiber-reinforced (e.g., Kevlar®, Twaron®, etc.) polymer-matrix composite materials and structures. These materials/structures are commonly used in various protective systems whose main requirement is a high level of mass-efficient penetration resistance against high kinetic energy projectiles (e.g., bullets, mine, IED or turbine fragments, etc.). Development of the aforementioned protection systems is traditionally carried out using legacy knowledge and extensive fabricate-and-test procedures. Since this approach is not only economically unattractive, but is often associated with significantly longer lead times, it has gradually become complemented by the appropriate cost- and time-efficient computer-aided engineering analyses. This trend has been accelerated by the recent developments in the numerical modeling of transient nonlinear dynamics phenomena such as those accompanying ballistic and blast-loading conditions.

M. Grujicic, B. Pandurangan, and J.S. Snipes, Department of Mechanical Engineering, Clemson University, 241 Engineering Innovation Building, Clemson, SC 29634-0921; and **C.-F. Yen, and B.A. Cheeseman**, Army Research Laboratory—Weapons & Materials Research Directorate, Aberdeen Proving Ground, MD 21005-5069. Contact e-mail: gmica@clemson.edu.

However, the tools used in these analyses themselves suffer from a number of deficiencies/limitations which prevent these analyses from being more widely utilized. One of the main deficiencies stems from the inability of currently available material models to realistically represent the response of these materials under high-deformation rate, large-strain, and high-pressure loading conditions, the conditions typically encountered during projectile impact events. One of the reasons for the indicated shortcomings of the (continuum-type) material models currently in use is a lack of inclusion of the contributions of various phenomena and processes occurring at different length scales to the overall behavior of the material under dynamic loading conditions. In the present study, an attempt is made to upgrade an existing high-rate composite material model through incorporation of the fine-scale microstructural (including defect) effects. Hence, the two main topics covered in the present study include (a) continuum-level composite material models; and (b) multi-length scale character of the composite-material microstructure. These topics are briefly reviewed in the remainder of this section.

1.1 Continuum-Level Composite Material Models

A review of the open literature, carried out as part of the present study, identified number of continuum-level material models for the composite materials under investigation. Some of these material models (e.g., Ref 1) focus on the role of various fiber/matrix damage processes solely due to in-plane loading. Since under common ballistic/blast-impact loading conditions, through-the-thickness normal and transverse shear stresses/strains are expected to play an important role, these types of models are of little utility in the computational analysis of protective structures. Among the material models which

Report Documentation Page			Form Approved OMB No. 0704-0188	
<p>Public reporting burden for the collection of information is estimated to average 1 hour per response, including the time for reviewing instructions, searching existing data sources, gathering and maintaining the data needed, and completing and reviewing the collection of information. Send comments regarding this burden estimate or any other aspect of this collection of information, including suggestions for reducing this burden, to Washington Headquarters Services, Directorate for Information Operations and Reports, 1215 Jefferson Davis Highway, Suite 1204, Arlington VA 22202-4302. Respondents should be aware that notwithstanding any other provision of law, no person shall be subject to a penalty for failing to comply with a collection of information if it does not display a currently valid OMB control number.</p>				
1. REPORT DATE MAR 2013	2. REPORT TYPE	3. DATES COVERED 00-00-2013 to 00-00-2013		
4. TITLE AND SUBTITLE Multi-Length Scale-Enriched Continuum-Level Material Model for Kevlar-Fiber-Reinforced Polymer-Matrix Composites			5a. CONTRACT NUMBER	
			5b. GRANT NUMBER	
			5c. PROGRAM ELEMENT NUMBER	
6. AUTHOR(S)			5d. PROJECT NUMBER	
			5e. TASK NUMBER	
			5f. WORK UNIT NUMBER	
7. PERFORMING ORGANIZATION NAME(S) AND ADDRESS(ES) Clemson University, Department of Mechanical Engineering, 241 Engineering Innovation Building, Clemson, SC, 29634			8. PERFORMING ORGANIZATION REPORT NUMBER	
9. SPONSORING/MONITORING AGENCY NAME(S) AND ADDRESS(ES)			10. SPONSOR/MONITOR'S ACRONYM(S)	
			11. SPONSOR/MONITOR'S REPORT NUMBER(S)	
12. DISTRIBUTION/AVAILABILITY STATEMENT Approved for public release; distribution unlimited				
13. SUPPLEMENTARY NOTES				
14. ABSTRACT				
15. SUBJECT TERMS				
16. SECURITY CLASSIFICATION OF:			17. LIMITATION OF ABSTRACT Same as Report (SAR)	18. NUMBER OF PAGES 15
a. REPORT unclassified	b. ABSTRACT unclassified	c. THIS PAGE unclassified	19a. NAME OF RESPONSIBLE PERSON	

include the contribution of all the attendant stress/strain components on the material response, most fall into the category of continuum damage mechanics models. In other words, damage is treated as a continuum-filled variable which evolves during loading and degrades locally the material's stiffness. Among these, the models which appear most noteworthy are (a) a plane-stress model for the composite materials reinforced with unidirectionally oriented fibers (Ref 2); (b) a fully three-dimensional composite-material model which accounts for the progressive character of the main fiber-damage modes, i.e., fiber fracture under axial tension, fiber buckling under compressive loading, fiber cutting under transverse shear, and fiber crushing under compressive through-the-thickness strains (Ref 3, 4); and (c) more recent three-dimensional (3D) composite material models which include various continuously distributed static intralamina and interlamina damage mechanisms (e.g., fiber breakage within the yarns, fiber/matrix de-bonding, diffuse delamination/interlamina separation, etc.) as well as discrete damage modes (e.g., transverse micro-cracking) (Ref 5-7).

The composite-material models briefly overviewed above all suffer from a common deficiency, i.e., they fail to account for the effects of high-loading rates under ballistic/blast impact conditions. This deficiency is removed in the composite material model proposed by Yen (Ref 8) when the contribution of the entire strain/stress field to all the main fiber and matrix failure modes is taken into account. This model is adopted in the present study, and an attempt is made to upgrade this model to include the effects of fine scale microstructure to the material response under dynamic loading conditions. Since this model is overviewed in great detail in section 2, it will not be discussed any further here.

1.2 Hierarchical/Multi-Length Scale Material Microstructure

Filament-based materials/structures under investigation are quite complex, and this complexity can be linked to the following main sources: (a) they contain a hierarchical/multi-length scale architecture; (b) their mechanical response is often quite nonlinear and rate/time-dependent; and (c) they are associated with a multiplicity of complex phenomena/processes (e.g., filament twisting, interfilament friction and sliding, etc.). In our recent studies (Ref 9, 10), an attempt was made to help us clarify the nature of the multi-length scale hierarchy of the fabric structures or fiber-reinforced composite materials under investigation. A set of eight length scales (described later) was established and briefly described. Schematics and explanations of the set of eight microstructural length scales is provided in Fig. 1. The first column in this figure shows a set of simple schematics of the material microstructure/architecture at a given length scale along with the labels used to denote the main microstructural constituents. In the second column, a brief description is provided of the material model used to capture the material behavior at the length scale in question. The key features of the material microstructure/architecture and the corresponding material model at each of the length scales listed in Fig. 1 can be summarized as follows: (a) *Laminate length-scale*: At this length scale, the material possesses no discernable microstructural features, i.e., it is completely homogenized. An example of the laminate-length scale composite material model can be found in Ref 11; (b) *Stacked-lamina length-scale*: At this length scale, the presence of discretely stacked laminae is recognized, while the material within each lamina as well as

interlamina boundaries are kept featureless/homogenized. An example of the composite material model at this length scale can be found in Ref 7; (c) *Single-lamina length-scale*: In this case, the microstructure/architecture of the reinforcement and matrix phases are explicitly taken into account, while the two associated materials are treated as featureless/homogenized. The resulting "two-phase" composite lamina model for each lamina is then combined with a fully homogenized lamina/lamina interface model to form a stackedlamina composite laminate structure. An example of this type of material model can be found in Ref 12; (d) *Fabric unit-cell length-scale*: At this length scale, a closer look is given to the architecture of the woven fabric. Specifically, details of yarn weaving and crimping, yarn cross-section change, and yarn sliding at the warp-yarn/weft-yarn cross-over points are taken into account. Each yarn is fully homogenized in this case as are the matrix and the lamina/lamina interfaces. An example of the model of this type can be found in Ref 13-15; (e) *Yarn length-scale*: In this case, the internal structure/architecture of each yarn is accounted for explicitly. In other words, yarns are considered as assemblies of nearly parallel fibers/filaments which are mechanically engaged by either the application of a light twist to the yarn or by wrapping a fiber around the fiber/filament assembly. Typically, the detailed microstructure of the yarns is not incorporated into material models used in large-scale simulations of projectile/protection-system impact interactions (due to the unmanageably large computer resources needed). Instead, computational results of the mechanical response of the individual yarns, when subjected to a variety of loading conditions, are used to enrich the homogenized material model for the yarns. The latter is subsequently used at the fabric unit-cell length scale. An example of this approach can be found in Ref 16; (f) *Fiber length-scale*: At this length scale, fibers are considered as assemblies of aligned long-chain molecules which are held together by non-bonding (van der Waals or Coulomb) forces. In the case of Kevlar® type fibers, there is a substantial experimental support (e.g., Ref 17) for the existence of fibrils within the fibers. Fibrils are smaller bundles of molecular chains within which chain molecules are tightly bonded into a perfect or nearly perfect crystalline phase. Thus, in the case of Kevlar® type fibers, fibers can be considered as an assembly of fibrils; (g) *Fibril-level length-scale*: As mentioned above, within the fibrils, the molecular structure is crystalline or nearly crystalline. However, as clearly demonstrated in our recent study (Ref 9), the material at this length scale (as well as the fiber length scale) may contain a variety of microstructural and topological defects and chemical impurities which may significantly alter its properties. As in the fiber length scale case, the material is treated as a collection of discrete interacting/bonded particles and analyzed using the atomic/molecular modeling tools/procedures; and (h) *Molecular chain-level length-scale*: At this length scale, chemical structure and conformation of the individual molecules constituting the chain are analyzed using the aforementioned atomic/molecular modeling tools/procedures. The main goal of the analysis at this length scale is to identify the most-likely molecular conformations present in the fibrils.

1.3 Objective

As mentioned earlier, the main objective of the present study is to identify and quantify fine-scale microstructural effects on the dynamic mechanical response of the composite materials

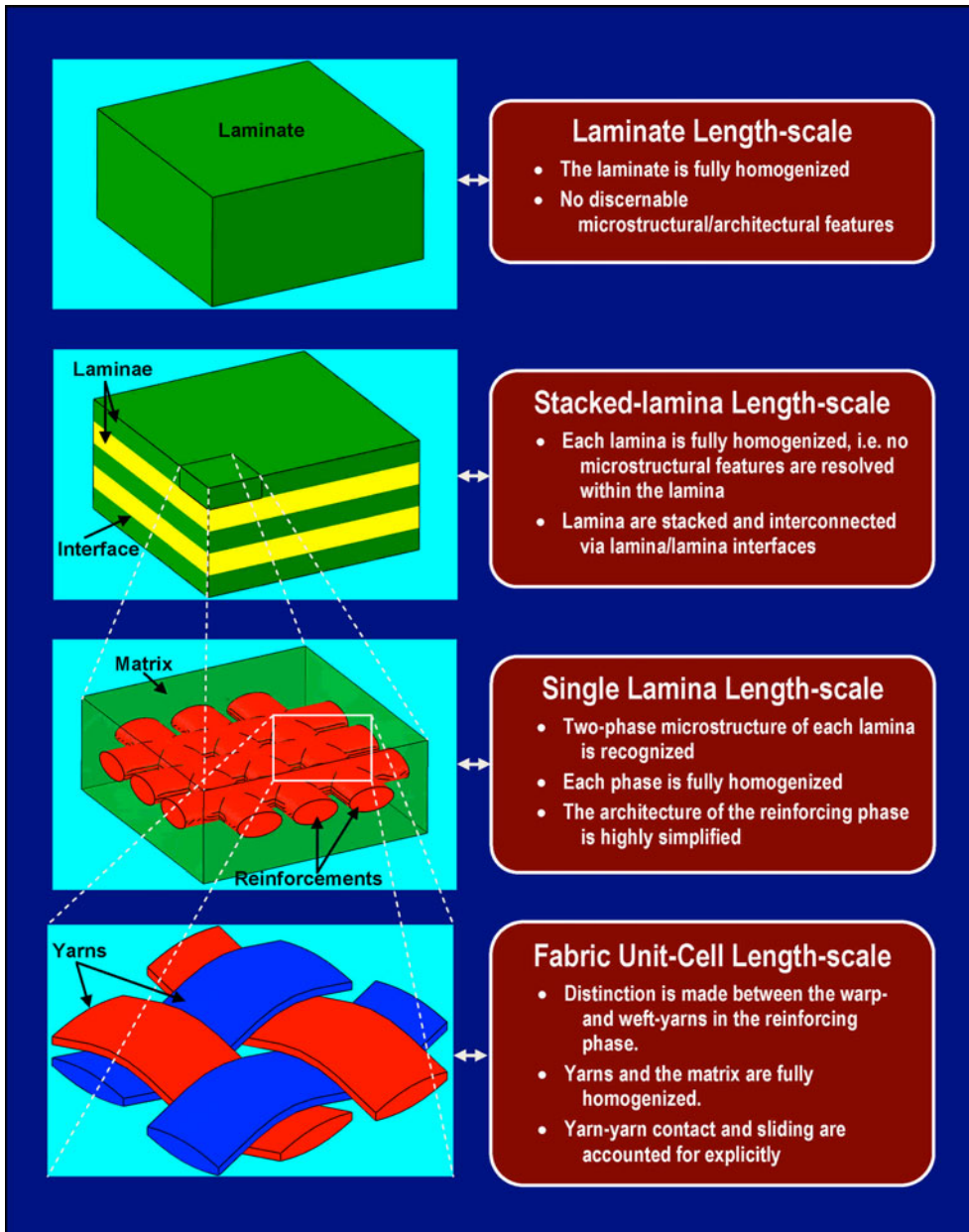


Fig. 1 Various length scales and the associated material model assumptions/simplifications used in the study of polymer-matrix composite materials with high-performance fiber-based structures

under investigation and to incorporate these effects into the continuum-level material model of Yen (Ref 8).

1.4 Organization of the Paper

A brief overview of the continuum-level composite material model proposed by Yen (Ref 8) is provided in section 2. A summary of the fiber and sub-fiber level microstructure and morphology of Kevlar®-based materials including the polymer-synthesis and fiber fabrication processes-induced defects is presented in section 3. The procedure used to upgrade the model of Yen (Ref 8) and the results obtained using the upgraded material model are all presented and discussed in section 4. The key findings resulting from the present study are summarized in section 5.

2. Overview of the Yen Composite Material Model (Ref 8)

In this section, a brief overview is provided of the rate-dependent composite material model developed by Yen (Ref 8). The defining features of this model can be summarized as follows:

- The model is an extension of the Hashin composite-material failure model (Ref 18) which more accurately accounts for the three-dimensional nature of the stress/strain states, high strain rates, and high pressures encountered during ballistic impact of composite laminates reinforced with plain-woven fabric;

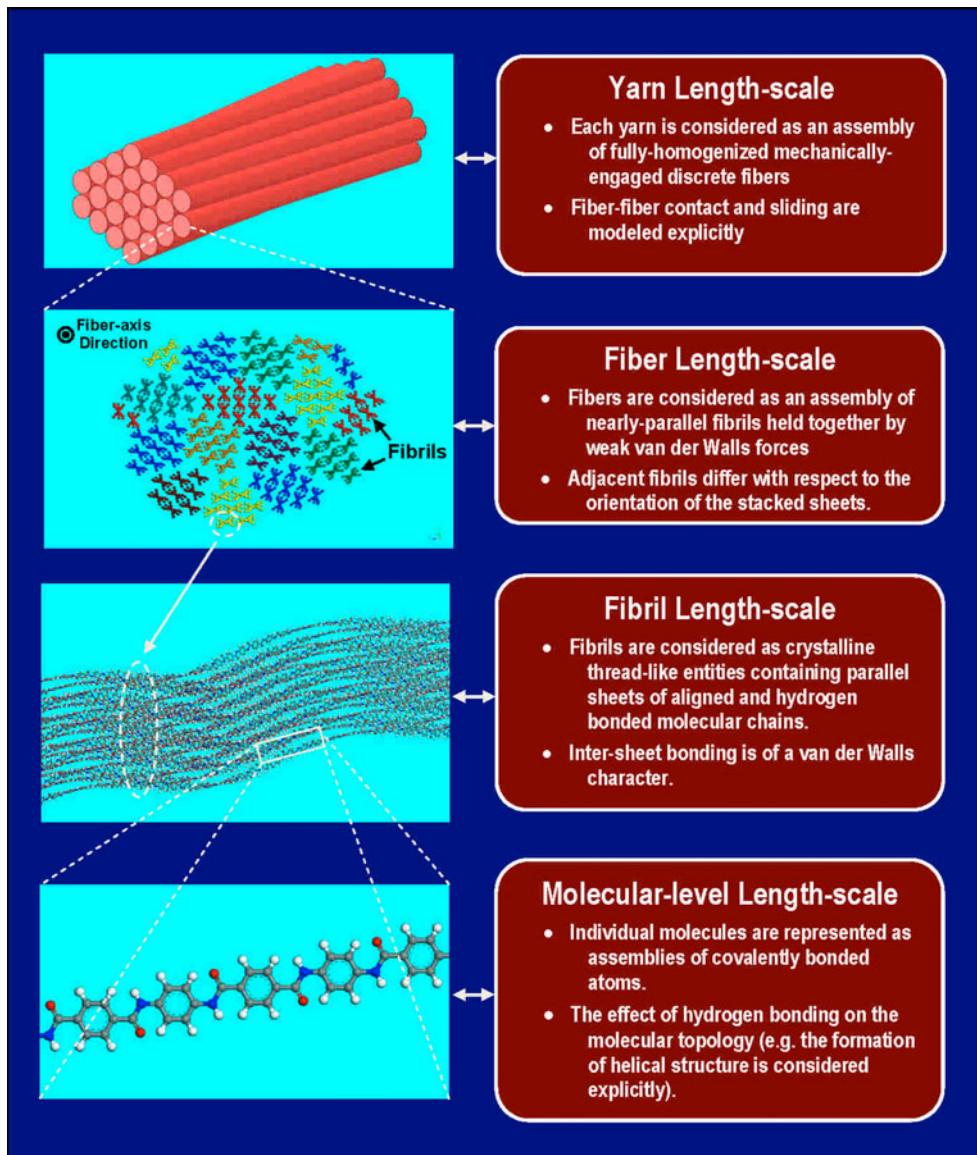


Fig. 1 continued

- (b) The material model is strain based and utilizes the concept of a ply/lamina-averaged local strain;
- (c) The model incorporates Mohr-Coulomb (Ref 19) shear strength effects, i.e., it accounts for the fact that the (matrix) in-plane shear strength is generally a function of the (tensile/compressive) character and magnitude of the through-the-thickness lamina strain;
- (d) Within the model, no distinction is made between fibers and yarns. Hence, to be consistent with the original model, in this section, the term “fiber” will be used to denote the thread-like entity which is used in the fabric-weaving process. In the next and the subsequent sections, the same entity will be referred to as a “yarn”;
- (e) The following three fiber and two matrix failure modes are considered: (i) fiber failure due to a combination of axial tensile and transverse shear strains; (ii) fiber buckling failure due to axial compressive strains; (iii) fiber crushing failure due to lamina through-the-thickness compressive strains; (iv) matrix in-plane shear failure;

and (v) matrix delamination failure due to a combined effect of the through-the-thickness tensile strains and transverse shear strains; and

- (f) The model is essentially of a linear-elastic orthotropic type with progressively degradable elastic stiffness constants. In other words, a generalized Hooke’s law relation is assumed to hold between stress and strain quantities, while damage is treated as a process which takes place gradually during ballistic impact. Consequently, the model relies on the definition of the damage initiation criteria and the corresponding damage evolution laws.

2.1 Damage Initiation Criteria

In this section, a brief overview is provided of the functional relations defining the onset (and continuation) of damage for each of the five aforementioned fiber/matrix failure modes. For each of the failure modes in question, as will be shown shortly, because distinction is made between weft and warp fibers, a set

of seven equations had to be used to fully describe damage initiation. Each of the seven equations has a general form: $f_i - r_i^2 = 0$ ($i = 1, \dots, 7$) where f_i represents the appropriate strain-based loading function, while r_i represents the corresponding strain-based damage threshold. Initially, each r_i is set to a value of 1.0 and, as a result of progressive damage, r_i values continue to increase.

It should be noted that in the remainder of this article, the following Cartesian coordinate system is used: x and y are, respectively, aligned with the weft and the warp fibers, while z is aligned in the composite-laminate through-the-thickness direction.

2.1.1 Fiber Damage Under Combined Axial Tension and Transverse Shear. The onset and progression of this failure mode is assumed to be defined by a superposition of the quadratic contributions of the axial tensile and transverse shear strains. For the weft and the warp fiber directions, the corresponding damage initiation functions can be written as

$$f_1 - r_1^2 = \left(\frac{E_x \langle \varepsilon_x \rangle}{S_{xT}} \right)^2 + \left(\frac{G_{xz} \varepsilon_{xz}}{S_{xFS}} \right)^2 - r_1^2 = 0 \quad (\text{Eq 1})$$

$$f_2 - r_2^2 = \left(\frac{E_y \langle \varepsilon_y \rangle}{S_{yT}} \right)^2 + \left(\frac{G_{yz} \varepsilon_{yz}}{S_{yFS}} \right)^2 - r_2^2 = 0 \quad (\text{Eq 2})$$

where E denotes the fiber Young's modulus, G the corresponding shear modulus, S the fiber strength, ε the relevant strain component, the Macaulay brackets $\langle \rangle$ are used to denote the ply/lamina-average local quantity, and subscripts T and FS denote, respectively, tension and fiber shear. It should be noted that in Eq 1 and 2, the laminate transverse shear strength is assumed to be controlled by the corresponding shear strength of the fiber itself.

2.1.2 Fiber Damage Under Axial Compression. The onset and progression of this failure mode is assumed to be defined by the compressive axial strains, effect of which is modulated by the lamina through-the-thickness compressive strain. In other words, axial compression-induced fiber buckling is resisted by the stabilizing effect of the through-thickness compressive strain. For the weft and the warp fiber directions, the corresponding damage initiation functions can be written as

$$f_3 - r_3^2 = \left[\frac{E_x \langle \varepsilon'_x \rangle}{S_{xC}} \right]^2 - r_3^2 = 0 \quad (\text{Eq 3})$$

$$f_4 - r_4^2 = \left[\frac{E_y \langle \varepsilon'_y \rangle}{S_{yC}} \right]^2 - r_4^2 = 0 \quad (\text{Eq 4})$$

where prime is used to denote modulation of the axial compressive strains as $\varepsilon'_x = -\varepsilon_x - \langle -\varepsilon_z \rangle (E_z/E_x)$ and $\varepsilon'_y = -\varepsilon_y - \langle -\varepsilon_z \rangle (E_z/E_y)$, and the subscript C denotes compression.

2.1.3 Fiber Damage Under Transverse Compressive Loading. This failure mode involves fiber crushing under sufficiently high through-the-thickness compressive strain, and its onset/progression is governed by the following equation:

$$f_5 - r_5^2 = \left(\frac{E_z \langle \varepsilon_z \rangle}{S_{FC}} \right)^2 - r_5^2 = 0 \quad (\text{Eq 5})$$

where the subscript FC denotes a fiber compression quantity.

2.1.4 Matrix In-plane Shear Failure. This mode of failure is associated with the fact that the matrix shear strength is lower than the fiber shear strength and that the composite

material in question possesses a laminated architecture. Consequently, sufficiently high in-plane shear strains may cause matrix shear failure without giving rise to any significant fiber damage. The onset and progression of this type of damage are governed by the following functional relationship:

$$f_6 - r_6^2 = \left(\frac{G_{xy} \varepsilon_{xy}}{S_{xy}} \right)^2 - r_6^2 = 0 \quad (\text{Eq 6})$$

2.1.5 Matrix Delamination due to Through-the-Thickness Tensile and Shear Stresses. This mode of failure also gives rise to the matrix in-plane failure, and its onset/progression is described by the following relation:

$$f_7 - r_7^2 = S^2 \left\{ \left(\frac{E_z \langle \varepsilon_z \rangle}{S_{zT}} \right)^2 + \left(\frac{G_{yz} \varepsilon_{yz}}{S_{yz0} + S_{SR}} \right)^2 + \left(\frac{G_{zx} \varepsilon_{zx}}{S_{zx0} + S_{SR}} \right)^2 \right\} - r_7^2 = 0 \quad (\text{Eq 7})$$

Examination of Eq 7 reveals the presence of three terms within the curly brackets on its right-hand side. The first term defines the contribution of tensile through-the-thickness strains, while the remaining terms represent the contributions of the transverse shear strains, to matrix delamination. In Eq 7, subscript 0 is used to denote the appropriate shear strength in the absence of the associated compressive normal strain, while subscript SR is used to denote an increase in this shear strength due to the presence of a normal compressive strain. The S_{SR} (sliding resistance term is assessed using the Mohr-Coulomb approach as

$$S_{SR} = E_z \tan \phi \langle -\varepsilon_z \rangle \quad (\text{Eq 8})$$

where $\tan \phi$ is the friction angle.

Equation 7 also contains a stress-concentration (scaling) factor, S . This factor is assigned a value larger than 1.0 in the non-delaminated portion of the material adjacent to the delamination boundary/front. This algorithm has been found to introduce enough flexibility into the model so that a better agreement can be obtained with the corresponding experimental results pertaining to the temporal evolution of the delamination zone (Ref 8);

2.2 Damage Evolution and Material Degradation

2.2.1 Damage Surface. Equations 1-7 given above define within the strain space a damage initiation/progression surface. Examination of these equations reveals that the material stiffness is characterized by three Young's moduli and three shear moduli. The initial damage initiation/progression surface is defined by substituting the initial values of the six moduli into Eq 1-7. As the material moduli degrade, the failure surface within the strain space expands (i.e., additional straining is required to produce additional damage). Within the composite material model developed by Yen (Ref 8), damage progression is assumed to cause degradation in material stiffness (without an accompanying loss in material strength) properties. The same assumption will be adopted in the present study. In our forthcoming study, however, it is planned to address the problem of strength degradation. It should be noted that although stiffness is considered as a non-degradable material property, it will be considered as a stochastic rather than a deterministic quantity in the present study.

2.2.2 Stiffness Degradation Variables. To account for the aforementioned damage-induced material-stiffness degradation, six stiffness degradation variables, ω_j ($j = 1, \dots, 6$), are

first introduced. Then, the effect of damage on the material elastic compliance matrix is described by the following relation (Ref 2):

$$[S] = \begin{bmatrix} \frac{1}{(1-\omega_1)E_x} & \frac{-v_{yx}}{E_y} & \frac{-v_{zx}}{E_z} & 0 & 0 & 0 \\ \frac{-v_{xy}}{E_x} & \frac{1}{(1-\omega_2)E_y} & \frac{-v_{zy}}{E_z} & 0 & 0 & 0 \\ \frac{-v_{xz}}{E_x} & \frac{-v_{yz}}{E_y} & \frac{1}{(1-\omega_3)E_z} & 0 & 0 & 0 \\ 0 & 0 & 0 & \frac{1}{(1-\omega_4)G_{xy}} & 0 & 0 \\ 0 & 0 & 0 & 0 & \frac{1}{(1-\omega_5)G_{yz}} & 0 \\ 0 & 0 & 0 & 0 & 0 & \frac{1}{(1-\omega_6)G_{zx}} \end{bmatrix} \quad (\text{Eq 9})$$

Finally, the “degraded” material elastic stiffness matrix is obtained by inverting the material elastic compliance matrix as defined by Eq 9. This procedure shows that to compute the instantaneous (degraded) material stiffness properties, one must know the corresponding values of the six stiffness degradation variables. To evaluate the same, one must define the appropriate evolution equations for the stiffness degradation variables.

Following Matzenmiller, et al. (Ref 2), the needed evolution equations are defined as

$$\dot{\omega}_j = \sum_i \dot{\phi}_i q_{ji} \quad (\text{Eq 10})$$

where $\dot{\phi}_i$ ($i = 1, \dots, 7$) denotes the rate of progression of each of the failure modes (the initiation of which was described by Eq 1-7), while q_{ji} represents a binary (0 or 1) two dimensional array with $j = 1, \dots, 6$ and quantifies the contribution of different failure modes to the evolution of stiffness degradation variables.

2.2.3 Damage Evolution Laws. Next, $\dot{\phi}_i$ functional relations are derived for each of the failure modes. It should be first noted that failure and the associated stiffness degradation are irreversible and that, during loading, an increase in the extent of damage of a given mode occurs only if the resulting strain increment crosses the corresponding failure surface, i.e., that the projection of the strain increment onto the local failure surface outward normal is positive as $\sum_k (\partial f_i / \partial \epsilon_k) \dot{\epsilon}_k > 0$, where $k (= 1, \dots, 6)$ is used to denote six components of the strain vector. Then, by defining the failure-mode-specific progression function, γ_i , the rate of progression of failure mode i can be defined as

$$\dot{\phi}_i = \sum_k \gamma_i \frac{\partial f_i}{\partial \epsilon_k} \dot{\epsilon}_k \quad (\text{Eq 11})$$

where no summation is implied over repeating indices. By choosing

$$\gamma_i = \frac{1}{2} (1 - \phi_i) f_i^{\frac{m}{2}-1} \quad (\text{Eq 12})$$

where the material parameter m quantifies the stiffness sensitivity to damage extent and noting that $\sum_k (\partial f_i / \partial \epsilon_k) \dot{\epsilon}_k = f$ the final expression for the rate of failure progression can be defined as

$$\dot{\phi}_i = \frac{1}{2} (1 - \phi_i) f_i^{\frac{m}{2}-1} \dot{f}_i \quad (\text{no summation over } i) \quad (\text{Eq 13})$$

2.2.4 Derivation of the Damage Coupling Matrix. To assemble the damage coupling matrix, q_{ji} (j denotes the elastic moduli, while i denotes the failure mode), the following approach was taken:

- (a) Failure of the weft and warp fibers both in tension and transverse shear and in compression degrades the associated Young's modulus and shear moduli;
- (b) Fiber crushing mode degrades all six elastic moduli;
- (c) In the case of the in-plane shear failure, only the associated shear modulus is affected; and
- (d) Delamination degrades the through-the-thickness Young's modulus as well as the two transverse shear moduli.

The resulting damage coupling matrix is

$$[q] = \begin{bmatrix} 1 & 0 & 1 & 0 & 1 & 0 & 0 \\ 0 & 1 & 0 & 1 & 1 & 0 & 0 \\ 0 & 0 & 0 & 0 & 1 & 0 & 1 \\ 1 & 1 & 1 & 1 & 1 & 1 & 0 \\ 0 & 1 & 0 & 1 & 1 & 0 & 1 \\ 1 & 0 & 1 & 0 & 1 & 0 & 1 \end{bmatrix} \quad (\text{Eq 14})$$

2.2.5 Integrated Form of the Stiffness Degradation Variables. By combining Eq 10, 12, and 13, the following expression is obtained for the contribution of the failure mode, i , to each stiffness degradation variable:

$$\omega_j = 1 - e^{\frac{1}{m}(1-r_i^m)}, \quad r_i \geq 1 \quad (\text{Eq 15})$$

Examination of Eq 15 reveals that initially, when r_i is equal to 1.0, the corresponding contribution to ω_j is zero. During loading, when the strain increment causes the strain to fall outside the damage surface associated with failure mode i , the corresponding damage surface crossed is expanded outward. This, in accordance with Eq 1-7, gives rise to an increase in r_i and, in turn, via Eq 15 to an increase in ω_j .

2.2.6 Residual Stiffness. According to Eq 15, at sufficiently high r_i , the stiffness degradation variable may acquire a value of 1.0 in which case the material completely loses the associated load carrying capacity. While this is physically realistic for some of the failure modes, e.g., the fiber failure under axial tension/transverse shear, it may not be fully realistic under other failure modes, e.g., fiber axial compression. Consequently, the following modifications are made in Eq 15:

(a) For the fiber axial compression failure mode:

$$\omega_j = \left(1 - e^{\frac{1}{m}(1-r_i^m)} \right) (1 - \eta_i), \quad i = 3 \text{ or } 4$$

$$\left\{ \begin{array}{l} \eta_3 \\ \eta_4 \end{array} \right\} = \left\{ \begin{array}{l} \frac{S_{i,\text{CR}}}{E_x \epsilon'_x} \\ \frac{S_{i,\text{CR}}}{E_y \epsilon'_y} \end{array} \right\} \quad (\text{Eq 16})$$

where the subscript R is used to denote the respective residual-strength quantities; and

(b) In the case of delamination failure mode, distinction is made between this failure mode under compressive and tensile through-the-thickness strains. In the former case, delamination surfaces are assumed to be closed, and Eq 15 for the two transverse shear moduli is modified to include the effect of the sliding resistance as

$$\left\{ \begin{array}{l} \omega_5 \\ \omega_6 \end{array} \right\} = \left(1 - e^{\frac{1}{m}(1-r_7^m)} \right) \left(1 - \frac{S_{\text{SR}}}{[(G_{yz}\epsilon_{yz})^2 + (G_{zx}\epsilon_{zx})^2]^{1/2}} \right) \quad (\text{Eq 17})$$

. On the other hand, in the case of the delamination under tensile through-the-thickness strains, no modifications are made to Eq 15.

2.3 Rate Dependency of Strength and Stiffness

As mentioned earlier, one of the defining features of the model developed by Yen (Ref 8) is the inclusion of material (strength and stiffness) rate dependency. To account for rate dependency of different components of material strength, the following scaling relation was used:

$$\{S_{RT}\} = \{S_0\} \left(1 + C_1 \ln \frac{\dot{\varepsilon}}{\dot{\varepsilon}_0} \right) \quad (\text{Eq 18})$$

where

$$\{S_{RT}\} = \begin{Bmatrix} S_{xT} \\ S_{yT} \\ S_{xC} \\ S_{yC} \\ S_{FC} \\ S_{xFs} \\ S_{yFs} \end{Bmatrix}, \quad \{\dot{\varepsilon}\} = \begin{Bmatrix} |\dot{\varepsilon}_x| \\ |\dot{\varepsilon}_y| \\ |\dot{\varepsilon}_z| \\ |\dot{\varepsilon}_{xy}| \\ |\dot{\varepsilon}_{yz}| \\ |\dot{\varepsilon}_{zx}| \end{Bmatrix},$$

C_1 is the strength rate constant, and the 6×1 column vector $\{S_0\}$ is equal to $\{S_{RT}\}$ when each of the relevant strain rates is equal to the single reference strain rate $\dot{\varepsilon}_0 = 1.0 \text{ s}^{-1}$.

The rate dependency of different stiffness components was accounted for in a similar fashion as

$$\{E_{rt}\} = \{E_0\} \left(1 + C_2 \ln \frac{\dot{\varepsilon}}{\dot{\varepsilon}_0} \right) \quad (\text{Eq 19})$$

where

$$\{E_{rt}\} = \begin{Bmatrix} E_x \\ E_y \\ E_z \\ G_{xy} \\ G_{yz} \\ G_{zx} \end{Bmatrix},$$

C_2 is the stiffness rate constant, and the 6×1 column vector $\{E_0\}$ is equal to $\{E_{RT}\}$ when each of the relevant strain rates is equal to the single reference strain rate $\dot{\varepsilon}_0 = 1.0 \text{ s}^{-1}$.

2.4 Material Model Parameterization

The material model presented above contains 14 strength parameters (S_{xT} , S_{yT} , S_{xFs} , S_{yFs} , S_{xC} , S_{yC} , S_{FC} , S_{xFs} , S_{yFs} , S_{zT} , S_{z0} , S_{xz0} , phi , S_{xCR} , and S_{yCR}), six stiffness parameters (E_x , E_y , E_z , G_{xy} , G_{yz} , and G_{zx}); two rate dependency parameters (C_1 and C_2), and two damage parameters (S and m). These parameters are commonly assessed by applying regression analysis to the results from a variety of mechanical tests over a range of strain rates. The large number of the model parameters makes this parameterization effort quite cumbersome, time consuming and costly. In addition, as will be discussed in the next section, some of these parameters are stochastic quantities and their complete specification requires the use of the appropriate probability distribution functions. Determination of these distribution functions is even more costly. Hence, a multi-length scale computational approach is introduced in the next section which allows establishment of the appropriate

distribution functions through the use of time-efficient, low cost computational methods and tools.

3. Microstructure/Property Relations in Kevlar® Fibers

In this section, a brief overview is provided of the basic microstructural features in Kevlar® at the fibril/fiber/yarn length scale(s), and their effects on the key material properties.

3.1 Fiber Crystalline Structure

Kevlar® (*p*-phenylene terephthalamide, PPTA) belongs to the family of polymeric materials known as polyamides. Polyamides are typically classified as aromatic polyamides or aramids (e.g., Kevlar®, the subject of the current study) and non-aromatic polyamides (e.g., Nylon 6,6). Kevlar® chains are inherently stiff and hence the chains do not readily flex. Consequently, in contrast to the flexible polymeric molecules which can undergo extensive folding and form the common (crystalline + amorphous) two phase structure, the Kevlar® fibers tend to typically form either a paracrystalline or a fully crystalline structure. The tendency for the formation of paracrystalline or crystalline structures is promoted by the presence of the planar phenylene and amide groups and by the ability of the adjacent chains to form hydrogen bonds. In the case of the paracrystalline structure, Kevlar® molecules are all aligned in the same direction but no order exists in a plane orthogonal to this direction. In sharp contrast, in the case of the fully crystalline Kevlar® fibers, molecules are aligned in all three mutually orthogonal directions.

The Kevlar® crystal structure is layered and consists of parallel (ABABAB...) stacked sheets formed due to the hydrogen bonding between the adjacent parallel Kevlar® molecules. The intersheet bonding on the other hand is mainly of the van der Waals (and p-electron weak chemical-bond) type. Owing to the relatively low strength of the van der Waals and the p-electron type weak intersheet bonding, Kevlar® fibers are prone to the formation of stacking faults and kink bands, and typically possess an inferior compressive strength and buckling resistance.

3.2 Common Defects in Kevlar® Fibers

As in most engineering materials, properties of Kevlar® fibers are greatly affected by the presence of various defects/flaws. These flaws can be introduced during Kevlar® synthesis and Kevlar® fiber fabrication processes. In our recent study (Ref 10), a detailed overview was provided of the main steps associated with Kevlar® synthesis and Kevlar® fiber processing. In the next section, a brief summary is provided of the commonly observed synthesis/processing-induced defects in Kevlar® fibers.

A summary of the Kevlar® fiber's most common defects, their dimensionality, their cause, methods of reducing their density, and their typical concentrations is provided in Table 1. Molecular-level schematics of these defects are displayed in Fig. 2(a)-(h). These defects are expected to have a profound effect on the fiber properties, as well as on the properties of coarser-scale materials and structures containing Kevlar® fibers (e.g., yarns, fabrics, plies, lamina, and laminates).

Table 1 A summary of the most common defects found in Kevlar®-based materials

Flaw group	Flaw	Causes	How causes can be remedied/mitigated	Range for concentration
Isolated chain ends (point defect)	-COOH	H ₂ SO ₄ catalyzed hydrolysis causing PPTA chain scission. Na ⁺ deficiency with respect to complete neutralization of side/end acidic groups	Use concentrated H ₂ SO ₄ for dope preparation. Shorten the fiber wash time	0.35 per PPTA chain for each flaw(a) (~ 350 ppm-mass-based)
	-NH ₂	H ₂ SO ₄ catalyzed hydrolysis causing PPTA chain scission. Na ⁺ deficiency with respect to complete neutralization of side/end acidic groups	Use higher concentration NaOH solution	0.35 per PPTA chain for each flaw(a) (~ 350 ppm-mass-based)
	-COO ⁻ Na ⁺	COOH neutralization with Na ⁺	No remedy required since this is one of the preferred chain ends	1.1 per PPTA chain(a) (~ 1100 ppm-mass-based)
	-NH ₃ ⁺ HSO ₄ ⁻	Sulfonation of the NH ₂ chain ends	Increase the H ₂ SO ₄ removal and neutralization rate	0.2 per PPTA chain(a) (~ 200 ppm-mass-based)
Side groups (point defect)	-SO ₃ H	Exposure of PPTA in the dope to concentrated H ₂ SO ₄ (sulfonation)	Reduce the H ₂ SO ₄ concentration in the dope	~1300 ppm (mass-based)
	-SO ₃ ⁻ Na ⁺	Neutralization of sulfonic acid side groups by NaOH	Remedy may not be required since this side group improves fiber longevity. However mechanical performance may be compromised	~2500 ppm (mass-based)
Voids and interstitials (point defects)	Microvoids	Swelling induced by hydration of intra-fibrillar Na ₂ SO ₄	Increase the extent of sodium salt dissolution by prolonged exposure of fibers to boiling water	~150 ppm (mass-based)
Defect bands (planar defects)	Mobile trapped H ₂ SO ₄	Non-neutralized or unwashed intra-fibrillar H ₂ SO ₄	Thorough washing in hot solvent aqueous bath	~70 ppm (mass-based)
	NH ₃ ⁺ HSO ₄ ⁻ agglomerated chain ends	Coulombic forces-induced clustering of ion-terminated chain ends	The phenomenon is not well understood so no remedy is obvious	One band every 40-60 nm of fibril (ca. 3000 ppm-mass-based)

(a) Extruded fibers

Consequently, a high-fidelity material model for Kevlar® fiber-reinforced composite materials must account for the presence, distribution, and potency of these defects in modifying material response under dynamic loading conditions. As mentioned earlier, the main objective of the present study is to upgrade one of the currently used continuum-level composite material models via incorporation of the effect of these defects.

3.3 Effect of Defects on Kevlar® Properties

In this section, a brief summary is provided of the main results obtained in our recent study (Ref 10) in which molecular-level modeling was used to establish the effects of various defects on the material properties (primarily strength and stiffness). In Ref 10, a procedure was introduced to establish relationships between topology/kinematics and properties of Kevlar® fibrils, fibers, and yarns, Fig. 3(a) and (b). In Fig. 3(a), a Kevlar® fiber is depicted, and it is shown that it consists of a number of nearly parallel fibrils. Within each of the fibrils, the fibril's axis lies within the Kevlar® sheets, and the fibrils merely differ in the orientation of the sheet normals (the sheet normal in each fibril is orthogonal to the fibril axis). Figure 3(b) displays the assumed relationship between the fibers and the yarns. Simply stated, the yarns are treated as

assemblies of nearly parallel fibers which are given a light twist to mechanically engage the fibers.

Within the analysis presented in Ref 10, it was assumed that the longitudinal stiffness, strength, and ductility of the fibrils make the dominant contribution to the corresponding fiber's and, in turn, yarn's properties. As far as the transverse strength of fibers and yarns are concerned, they are expected to be controlled by weak interfibril (and in the case of yarns, weak interfiber) van der Waals/mechanical interlocking forces and to be less dependent on the fibril's transverse mechanical properties.

The results obtained in Ref 10 can be summarized as follows: (a) fibril's stiffness was found to be affected by both the type and concentration of the defects. An example of the typical results pertaining to the effect of defect type/concentration on the Kevlar fibril's stiffness is depicted in Fig. 4(a) and (b). In Fig. 4(a), the case of -COOH chain end defect is considered, while, in Fig. 4(b), the case of -SO₃H side group defect is analyzed; (b) As far as the fibril's axial strength is concerned, it was found to be affected by defect type and the size and composition of the largest defect cluster. Examples of typical results obtained are shown in Tables 2 and 3. The clusters composed of defects of the same type are depicted in Table 2, while the effect of mixed-type defect (chain end and

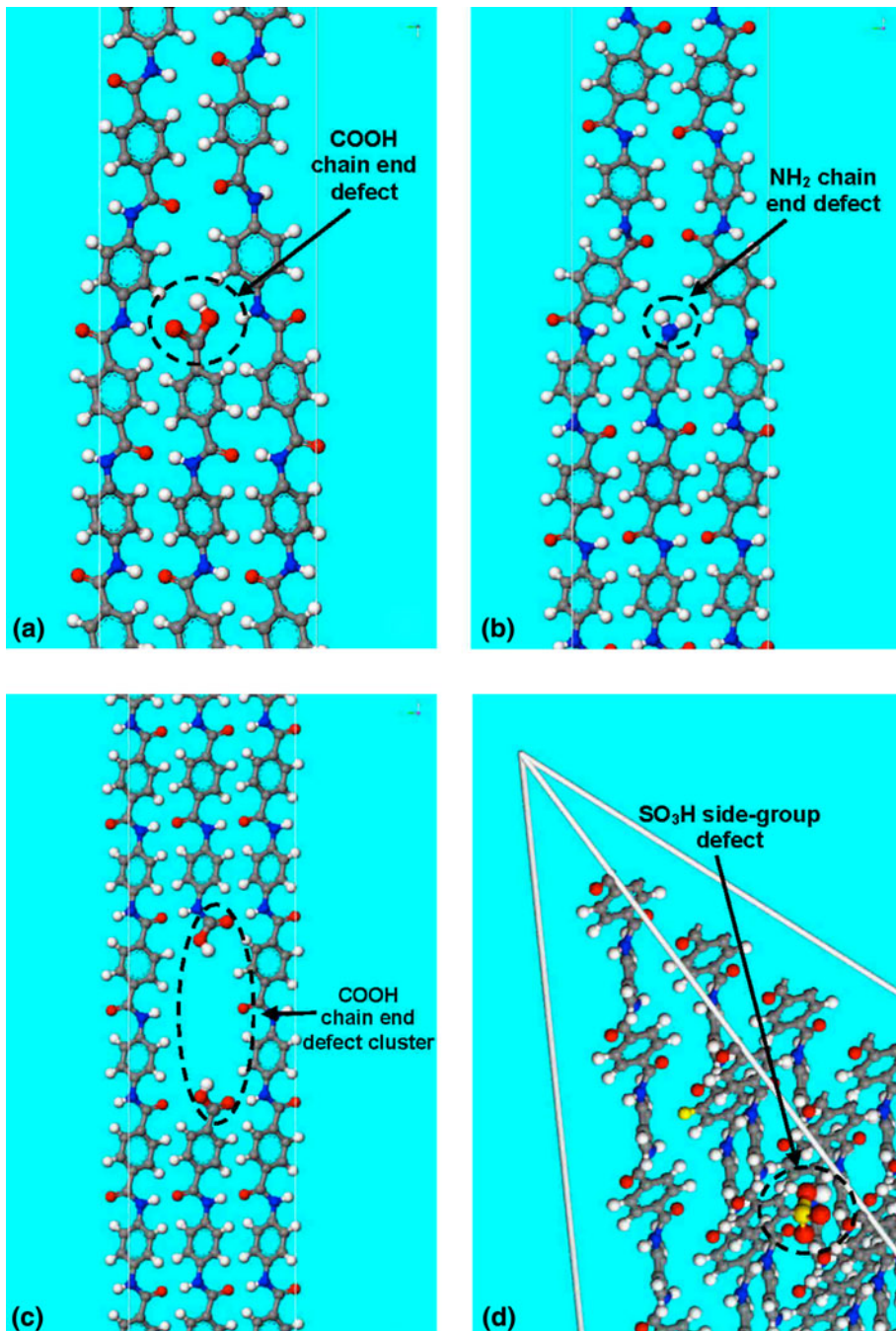


Fig. 2 Examples of the molecular-level defects in Kevlar® fibers: (a) a COOH chain-end defect; (b) a NH₂ chain-end defect; (c) a COOH chain-end defect cluster; (d) a SO₃H side-group defect; (e) a SO₃H side-group defect cluster; (f) a microvoid defect; (g) a H₂SO₄ interstitial defect; and (h) a collection of chain ends forming a defect band

side group) clusters is depicted in Table 3. An examination of the results reported in Tables 2 and 3 reveals that the extent of the loss of fibril's axial strength increases with the cluster size/strength; (c) The aforementioned finding that the fibril's axial strength is a function of the largest defect cluster and its composition indicated that fibril's strength is a stochastic property. Hence, in Ref 10, results like those displayed in Tables 2 and 3 are combined with the prototypical defect concentration densities, Table 1, to derive the associated Kevlar® fibril-strength distribution function, Fig. 5(a) and (b); (d) In accordance with Fig. 3(a), Kevlar® fibers are assumed to

be transversely isotropic (with the fiber axis being the unique material direction) although the constituent fibrils possess orthotropic symmetry. Consequently, (i) fiber axial stiffness and strength, E_{11} , and σ_1 are set equal to their fibril's counterparts; (ii) the fiber transverse normal stiffness, $E_{22} = E_{33}$, is set equal to the more compliant E_{33} fibril's modulus; (iii) all the three shear moduli G_{12} , G_{13} , and G_{23} are set equal to the same value which is controlled by the compliant Kevlar® intersheet sliding resistance (i.e., G_{12} of the fibrils); and (e) To assess the yarn-level stiffness and strength properties from the known fiber properties, additional effects arising from the

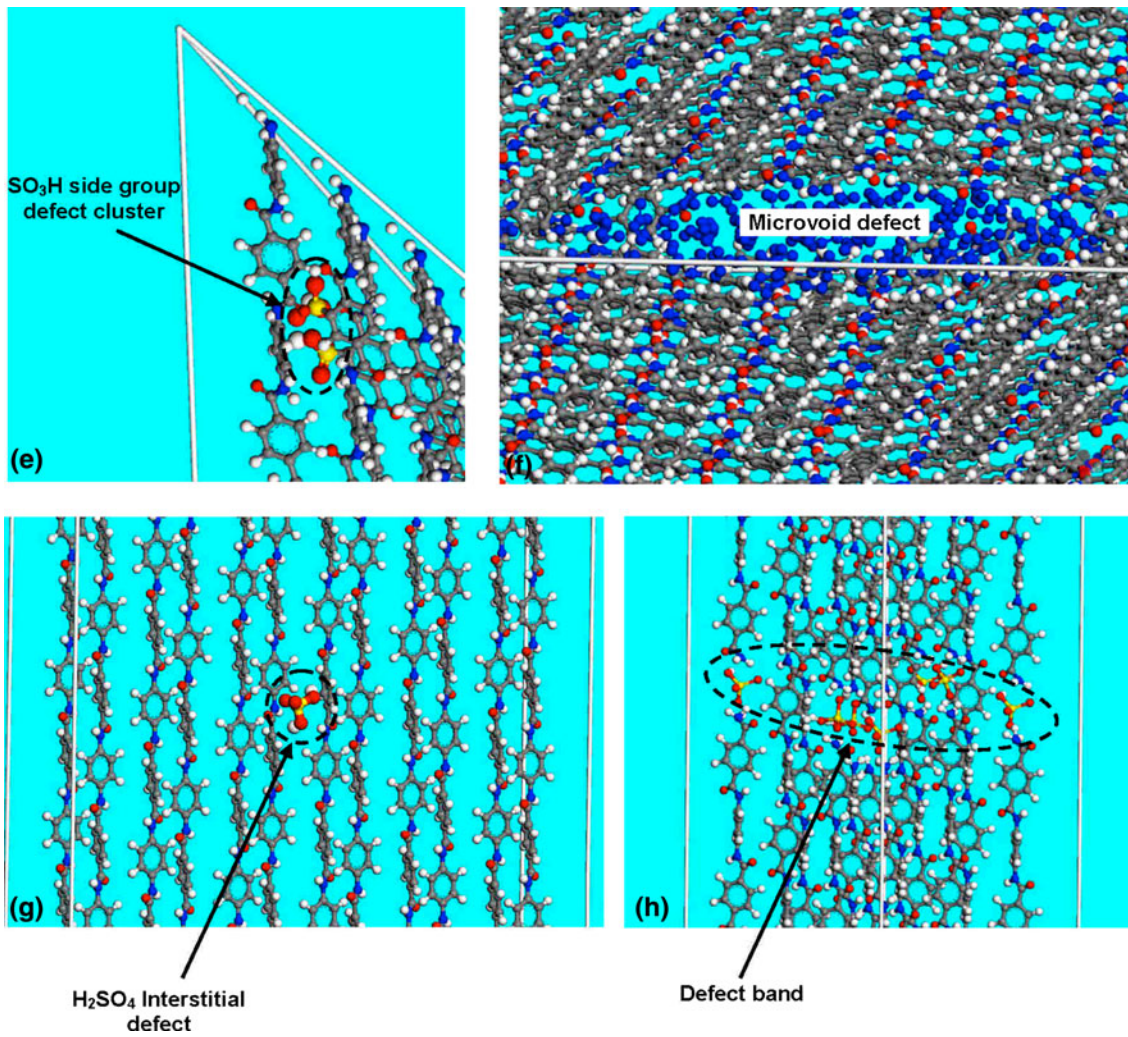


Fig. 2 continued

fiber-twist-induced interfiber friction had to be taken into account. This procedure mainly affected the yarn axial strength (or more precisely, yarn axial strength distribution). It was generally found that the fibril-level axial strength distribution function displayed in Fig. 5(a) and (b) was modified in the yarn case by an interfiber friction dependent (positive) strength shift. For example, for a prototypical extent of fiber twist, an increase in the strength of ca. 0.2 GPa was found.

4. Enrichment of Yen (Ref 8) Composite Material Model

In this section, some of the findings/results reported in section 3 are used to enrich the continuum-level material model developed by Yen (Ref 8). Specifically, Kevlar®-fiber's strength distribution functions like the one displayed in Fig. 5(a) and (b) are used to impart a stochastic character to the Kevlar®-fiber's tensile strength and transverse-shear strength parameters S_{xT} , S_{yT} , S_{xFS} , and S_{yFS} . It should be recalled that these strength parameters are treated, both in the material model developed by Yen (Ref 8) and in its present modification, as non-degradable material properties. To demonstrate the effect of material model

modifications on the material mechanical response, the case of uniaxial tension in the weft direction is first considered. This is followed by a dynamic computational analysis in which a rigid projectile of a right circular cylindrical geometry is impacting, at a zero obliquity angle, a target laminate of rectangular-parallelepiped geometry. In the latter case, it was critical to demonstrate how much the proposed material-model modifications can affect the composite laminate computed ballistic limit, as quantified by the V_{50} (the projectile incident velocity at which the probability of target penetration is 50%).

4.1 Uniaxial Tension Test

In this section, a quasi-static uniaxial tension test is simulated using the conventional finite element method. Details of the finite element procedure used are identical to the one reported in our prior study (Ref 11, 20-22). In short, a rectangular-parallelepiped-shaped composite-material test sample with its longitudinal axis aligned in the weft direction is subjected to a progressively larger axial strain (while no lateral constraints are imposed, to attain a uniaxial stress state condition). To identify differences in the tensile-response of the test sample brought about by the proposed modifications in the material model, various global-response and spatial distributions of material

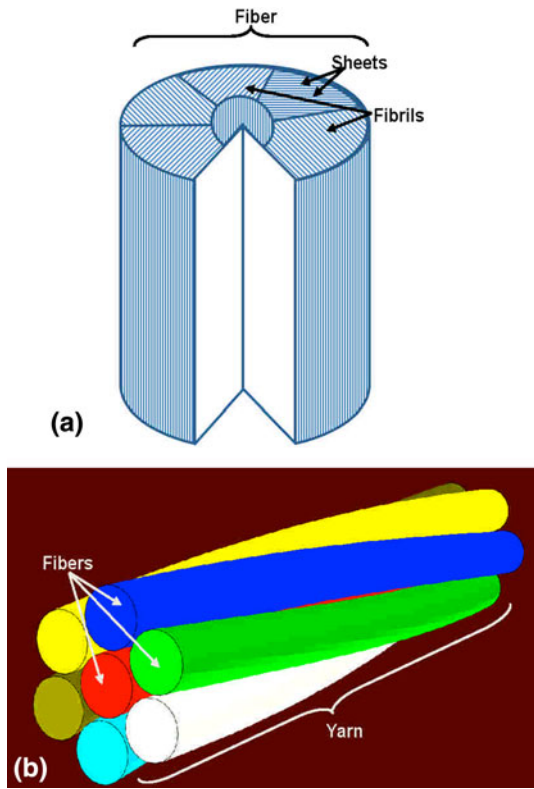


Fig. 3 Topological relationships between (a) fibrils and fibers; and (b) fibers and yarns adopted in the present investigation

state variables are monitored/generated. Details of the results obtained are presented below.

A comparison of the uniaxial tension (loading) true stress versus uniaxial tension true strain curves for a prototypical Kevlar® plain woven composite material obtained using the original Yen (Ref 8) material model and its upgrade proposed in the present study is shown in Fig. 6. Examination of this figure reveals that

(a) almost up to the onset of failure, the two curves are effectively coincident; (b) However, the composite updated material model shows that the onset of failure occurs at a 3-4% lower stress level and a slightly smaller strain; and (c) The updated material model predicts a higher rate of material damage/degradation. In other words, the material displays almost a brittle-like behavior.

In Fig. 7(a)-(d) and 8(a)-(d), a comparison is made between temporal evolutions of spatial distribution of the axial tensile stress in the weft direction in the same prototypical Kevlar® plain woven composite material, obtained using the original Yen (Ref 8) material model and the updated material model proposed in the present study. An examination of these results reveals that, at each level of the imposed overall axial tensile strain, the spatial distribution of the axial tensile stress is fairly uniform. This finding is somewhat influenced by the choice of the stress scale (100-600 MPa) used in these figures. In other words, to obtain distinct colors for specific stress levels over the entire loading cycle, a constant/common stress range was used.

In Fig. 9(a) and (b), a comparison is made between spatial distribution of the axial tensile stress in the weft direction in the same prototypical Kevlar® plain woven composite material, obtained using the original Yen (Ref 8) material model and the

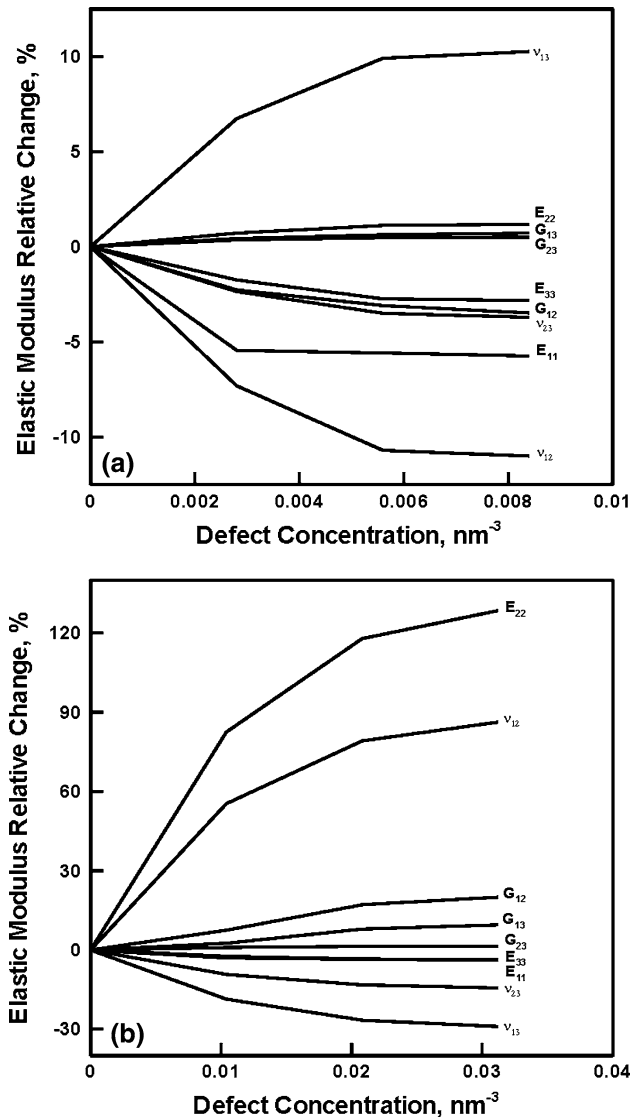


Fig. 4 The effect of the concentration of the (a) $-COOH$ chain end group; and (b) $-SO_3H$ side group on the orthotropic elastic stiffness constants of the Kevlar® fibrils

updated material model proposed in the present study at the instant when the overall/average axial stress experiences a maximum. An examination of the results displayed in these figures shows that, while in the case of the original Yen (Ref 8) material model, Fig. 9(a), spatial distribution of the axial stress is indeed quite uniform, in the case of the upgraded composite material model the axial-stress distribution is somewhat nonuniform. To explain these differences, a comparison is made in Fig. 10(a) and (b) between the spatial distributions of the extent of axial tension/transverse shear damage in the weft direction in Kevlar® plain woven composite material using the original Yen (Ref 8) material model and the updated material model proposed in the present study at the instant when the overall/average axial stress experiences a maximum. It is seen that, while in the case of original Yen (Ref 8) material model this damage variable is fairly uniformly distributed (and equal to zero), in the case of the updated material model, one of the ten cubic finite elements constituting the tensile specimen has acquired a non-zero value of this damage variable. This finding

Table 2 A summary of the effect of the most common defects found in Kevlar®-based materials and their (same defect-type) clusters on the PPTA fibril's axial tensile strength (in GPa)

Flaw group	Flaw	Number of defects in the largest cluster		
		1	2	3
Isolated chain ends (point defect)	-COOH	6.0	5.6	5.0
	-COO ⁻ Na ⁺			
Side groups (point defect)	-NH ₂	6.1	5.8	5.2
	-NH ₃ ⁺ HSO ₄ ⁻			
Voids and interstitials (point defects)	-SO ₃ H	5.8	5.1	4.1
	-SO ₃ ⁻ Na ⁺			
Defect bands (planar defects)	Microvoids	3.8	N/A	N/A
	Mobile Trapped H ₂ SO ₄	3.9	N/A	N/A
	NH ₃ ⁺ HSO ₄ ⁻ agglomerated chain ends	3.2	N/A	N/A

Table 3 A summary of the effect of the composition and the size of the mixed SO₃H/SO₃⁻Na⁺ based side group and COOH/COO⁻Na⁺ based chain end defect clusters on the PPTA fibril's axial tensile strength (in GPa)

	Number of SO ₃ H/SO ₃ ⁻ Na ⁺ defects in the cluster		
	1	2	3
Number of COOH/COO ⁻ Na ⁺ defects in the cluster			
1	5.5	4.8	3.8
2	5.3	4.4	3.4
3	4.5	3.8	2.7

explains not only the axial-stress nonuniformities observed in Fig. 9(b) but also the more brittle nature of the composite material. In other words, once one of the elements acquires a non-zero value of the uniaxial tension/transverse shear damage variable, further deformation becomes localized within this element. This causes both the structural weakening of the material in this element (due to loss of the associated Young's modulus) and the geometrical weakening (due to a reduction in the cross-sectional area supporting the applied axial load). It should be noted that the observed differences between the results presented in Fig. 9(a) and (b), as well as the differences between the results presented in Fig. 10(a) and (b), are due to the stochastic nature of material strength parameters implemented into the updated material model. In other words, the failed element identified in Fig. 9(b) and 10(b) is associated with the lowest level of tensile strength.

The results displayed in Fig. 6–10 clearly reveal that incorporation of the realistic micro-mechanics effects such as the operation of various fiber/matrix-damage mechanisms and the stochastic nature of the material strength can significantly alter the global as well as the local response of the material to the imposed loading. While this finding can be considered as expected, its direct quantitative experimental validation is quite challenging and is beyond the scope of the present study.

4.2 Lamine Transverse Impact by a Rigid Cylindrical Projectile

In this section, the problem of composite laminate transverse impact by a right circular cylindrical rigid projectile is analyzed

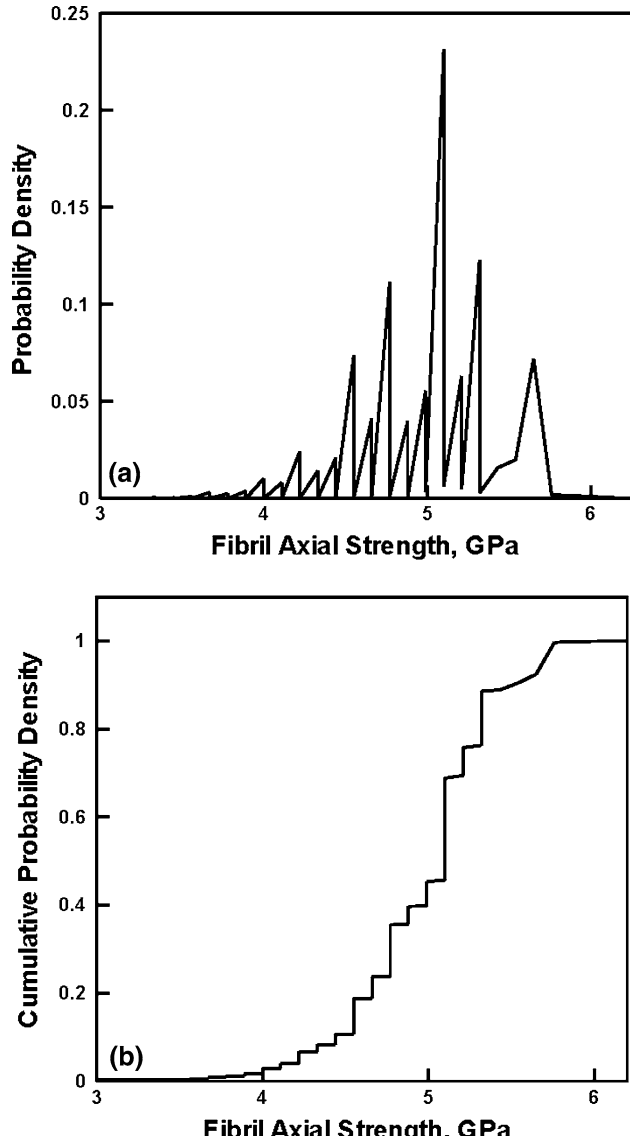


Fig. 5 (a) Kevlar®-fibril's axial strength probability density function; and (b) the corresponding cumulative distribution function determined in the present study using molecular-type computational analyses

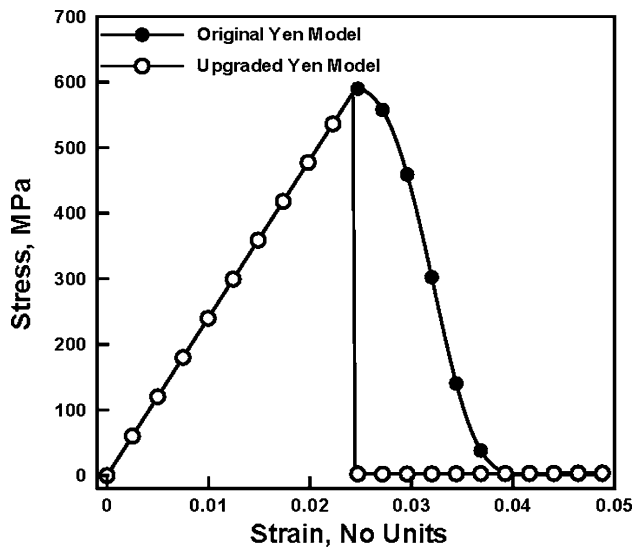


Fig. 6 A comparison of the uniaxial tensile true stress vs. uniaxial tensile true strain behavior (in the weft direction) in a prototypical Kevlar® plain woven composite material obtained using the original Yen (Ref 8) material model and its upgrade proposed in the present study

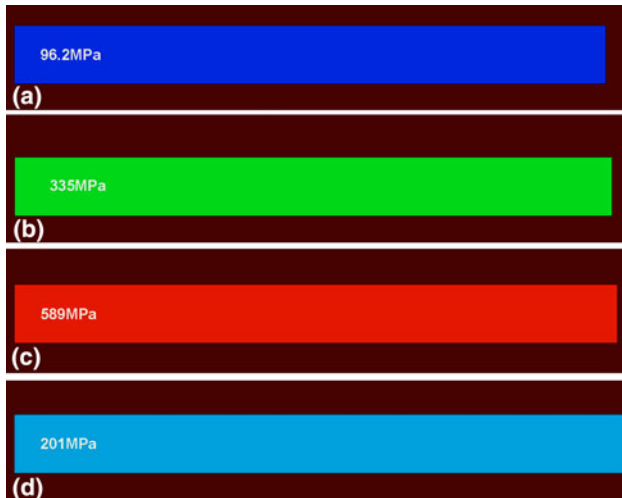


Fig. 7 Spatial distribution of the axial tensile stress in the weft direction in a prototypical Kevlar® plain woven composite material obtained using the original Yen (Ref 8) material model at the average axial strain levels of (a) 0.004; (b) 0.014; (c) 0.024; and (d) 0.033

using a dynamic explicit finite element computational analysis. Since details of the finite element procedure used is identical to the one reported in our prior study (Ref 11), they will not be repeated here.

An example of the prototypical results obtained in the present study is given in Fig. 11(a)-(d). The results displayed in Fig. 11(a)-(d) pertain to the spatial distribution of the composite-laminate material during impact. It should be noted that to enable monitoring of the penetration process, the target plate is made transparent. The results displayed in Fig. 11(a)-(d) clearly reveal the development of the back face bulge. In general, it was found that details regarding the spatial distribution and the

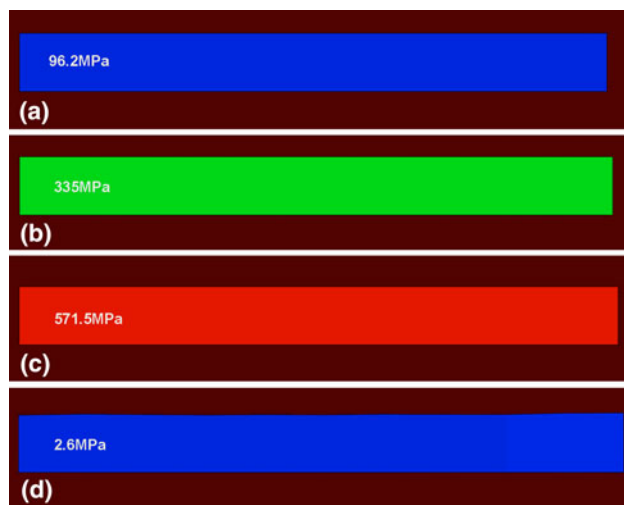


Fig. 8 Spatial distribution of the axial tensile stress in the weft direction in a prototypical Kevlar® plain woven composite material obtained using the upgraded model proposed in the present study at the average axial strain levels of (a) 0.004; (b) 0.014; (c) 0.024; and (d) 0.032

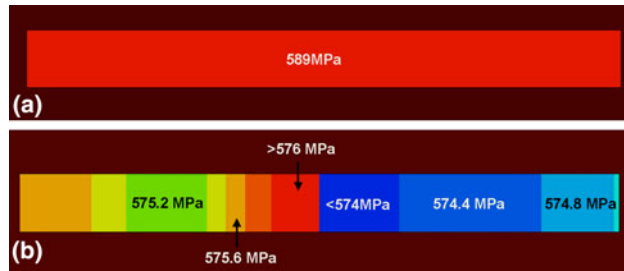


Fig. 9 A comparison between the spatial distributions of the axial tensile stress in the weft direction in Kevlar® plain woven composite material at the instant when the overall/average axial stress experiences a maximum, obtained using (a) the original Yen (Ref 8) material model; and (b) the updated material model proposed in the present study

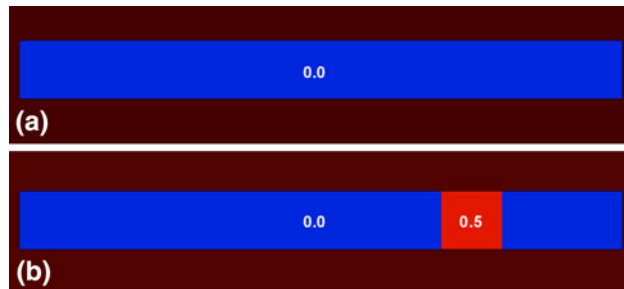


Fig. 10 A comparison between the spatial distributions of the extent of axial tension/transverse shear damage in the weft direction in Kevlar® plain woven composite material at the instant when the overall/average axial stress experiences a maximum, obtained using (a) the original Yen (Ref 8) material model; and (b) the updated material model proposed in the present study

temporal evolution of the target material during impact are affected by the modifications made to the original Yen (Ref 8) composite material model. Details regarding the effect of these

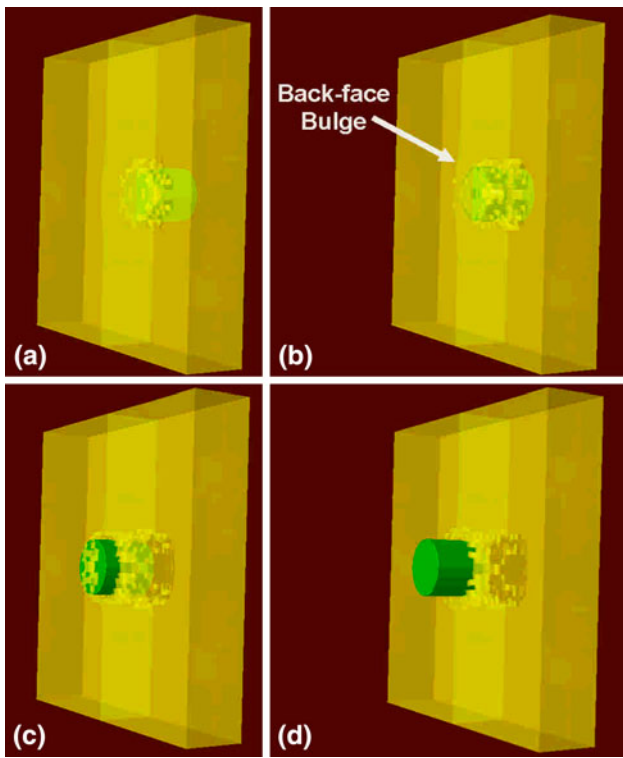


Fig. 11 Typical results pertaining to the temporal evolution of the spatial distribution of the composite-laminate material during impact by a right-circular cylindrical rigid projectile

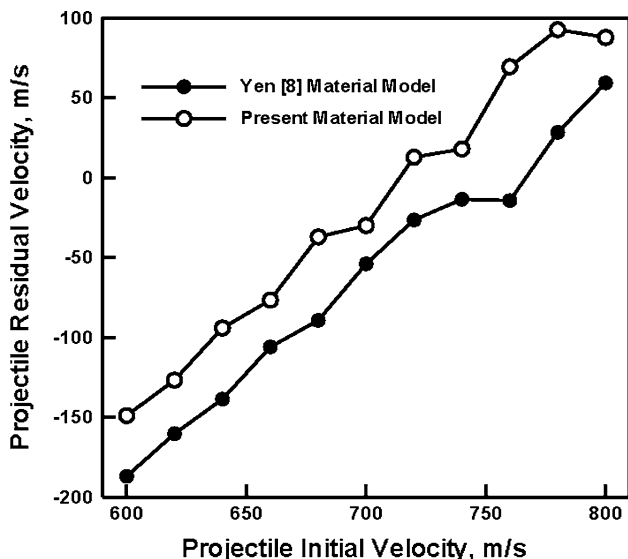


Fig. 12 A typical projectile residual velocity vs. projectile incident velocity plot showing differences in V_{50} as predicted by the original Yen (Ref 8) material model and its upgrade proposed in the present study

material model modifications on the temporal evolution and spatial distribution of the target-material and its various mechanical and microstructural fields will be presented in our future communication. In the remainder of this section, results pertaining to the effect of material model modifications on V_{50} are presented and discussed.

Typical results pertaining to the effect of projectile initial velocity on the projectile residual velocity in the case of the original Yen (Ref 8) composite material model and its present modification are displayed in Fig. 12. It is seen that V_{50} (defined here as the projectile initial velocity at which the projectile residual velocity is zero) predicted by the analysis in which the modified composite material model is used is ca. 5% lower than its counterpart associated with the use of the original Yen (Ref 8) composite material model. This effect is deemed as being significant and justifies the present efforts aimed at incorporating fine-scale microstructural effects into the continuum-level material model. However, no relevant experimental data are presently available to be able to judge the potential improvements in the experiment/calculation agreement brought about by the use of the modified composite material model. This deficiency in the relevant experimental data will be addressed in our future study.

5. Summary and Conclusions

Based on the results obtained in the present study, the following summary remarks and main conclusions can be drawn:

1. A continuum-level rate-dependent material model for plain woven Kevlar®-fiber-reinforced polymer matrix composite has been upgraded by incorporating the effects of fibril/fiber/yarn level microstructure phenomena and processes.
2. Specific microstructural effects incorporated into the continuum-level material model account for the role of various material synthesis/fiber processing-induced defects on the material strength, or more specifically on the material strength distribution function.
3. For a prototypical plain woven Kevlar®-fiber-reinforced polymer matrix composite, the results obtained using a series of finite element analyses show that the predicted response of the material both under quasi-static and dynamic ballistic-impact conditions is significantly affected as a result of the incorporation of microstructural effects.

Acknowledgments

The material presented in this article is based on research supported by the Army Research Office (ARO) research contract entitled “Multi-length-scale Material Model Development for Armor-grade Composites” (Contract Number W911NF-09-1-0513) and the Army Research Laboratory (ARL) research contract entitled “Computational Analysis and Modeling of Various Phenomena Accompanying Detonation Explosives Shallow-Buried in Soil” (Contract Number W911NF-06-2-0042). The authors are indebted to Dr. Larry Russell of ARO for his continuous support and interest during the above study.

References

1. F.K. Chang and K.Y. Chang, A Progressive Damage Model for Laminated Composites Containing Stress Concentration, *J. Compos. Mater.*, 1987, **21**, p 834–855

2. A. Matzenmiller, J. Lubliner, and R.L. Taylor, A Constitutive Model for Anisotropic Damage in Fiber-Composites, *Mech. Mater.*, 1995, **20**, p 125–152
3. K. William and R. Vaziri, Finite Element Analysis of the Impact Response of CFRP Composite Plates, *Proceedings of the ICCM-11*, Gold Coast, 1995, p 532–654
4. J. Van Hoof, M.J. Woeswick, P.V. Straznicky, M. Bolduc, and S. Tylko, Simulation of Ballistic Impact Response of Composite Helmets, *Proceedings of the 5th International LS-DYNA Users Conference*, Southfield, 1998
5. P. Ladeveze, Multiscale Computational Damage Modelling of Laminate Composites, *Multiscale Modeling of Damage and Fracture Processes in Composite Materials*, T. Sadowski., Ed., Springer, New York, 2005, p 309
6. P. Ladeveze, G. Lubineau, and D. Violeau, A Computational Damage Micromodel of Laminated Composites, *Int. J. Fract.*, 2006, **137**, p 139–150
7. M. Grujicic, T. He, H. Marvi, B.A. Cheeseman, and C.F. Yen, A Comparative Investigation of the Use of Laminate-Level Meso-Scale and Fracture-Mechanics-Enriched Meso-Scale Composite-Material Models in Ballistic-Resistance Analyses, *J. Mater. Sci.*, 2010, **45**, p 3136–3150
8. C.F. Yen, A Ballistic Material Model for Continuous-Fiber Reinforced Composites, *Int. J. Impact Eng.*, 2012, **46**, p 11–22
9. M. Grujicic, W.C. Bell, P.S. Glomski, B. Pandurangan, C.-F. Yen, and B.A. Cheeseman, Filament-Level Modeling of Aramid-Based High Performance Structural Materials, *J. Mater. Eng. Perform.*, 2011, **20**, p 1401–1413
10. M. Grujicic, B. Pandurangan, C.-F. Yen, and B.A. Cheeseman, Multi-length-scale Computational Derivation of Kevlar® Yarn-Level Material Model, *J. Mater. Sci.*, 2011, **46**, p 4787–4802
11. M. Grujicic, B. Pandurangan, K.L. Koudela, and B.A. Cheeseman, A Computational Analysis of the Ballistic Performance of Light-Weight Hybrid-Composite Armor, *Appl. Surf. Sci.*, 2006, **253**, p 730–745
12. M. Grujicic, D.C. Angstadt, Y.-P. Sun, and K.L. Koudela, Micro-Mechanics Based Derivation of the Materials Constitutive Relations for Carbon Nanotube Reinforced Poly-Vinyl-Ester-Epoxy Based Composites, *J. Mater. Sci.*, 2007, **42**, p 4609–4623
13. M. Grujicic, G. Arakere, T. He, M. Gogulapati, and B.A. Cheeseman, A Numerical Investigation of the Influence of Yarn-Level Finite-Element Model on Energy Absorption by a Flexible-Fabric Armor During Ballistic Impact, *J. Mater. Des. Appl.*, 2008, **222**, p 259–276
14. M. Grujicic, W.C. Bell, G. Arakere, T. He, X. Xie, and B.A. Cheeseman, Development of a Meso-Scale Material Model for Ballistic Fabric and its Use in Flexible-Armor Protection Systems, *J. Mater. Eng. Perform.*, 2010, **19**(1), p 22–39
15. M. Grujicic, W.C. Bell, T. He, and B.A. Cheeseman, Development and Verification of a Meso-Scale Based Dynamic Material Model for Plain-Woven Single-Ply Ballistic Fabric, *J. Mater. Sci.*, 2008, **43**, p 6301–6323
16. B.A. Cheeseman, C.F. Yen, B.R. Scott, B. Powers, T.A. Bogetti, B. LaMatina, Y. Duan, M. Keefe, Y. Miao, and Y. Wang, “From Filaments to Fabric Packs—Simulating the Performance of Textile Protection Systems,” ARL Report ADM002075, 2006
17. S.M. Lee, *Handbook of Composite Reinforcements*, Wiley, New York, 1993, ISBN 978-0-471-18861-2
18. Z. Hashin, Failure Criteria for Unidirectional Fiber Composites, *J. Appl. Mech.*, 1980, **47**, p 329–334
19. A. Puck and H. Schurmann, Failure Analysis of FRP Laminates by Means of Physical Based Phenomenological Models, *Compos. Sci. Technol.*, 1998, **58**, p 1001–1010
20. M. Grujicic, W.C. Bell, B. Pandurangan, and T. He, Blast-Wave Impact-Mitigation Capability of Polyurea When Used as Helmet Suspension Pad Material, *Mater. Des.*, 2010, **31**, p 4050–4065
21. M. Grujicic, B. Pandurangan, R. Qiao, B.A. Cheeseman, W.N. Roy, R.R. Skaggs, and R. Gupta, Parameterization of the Porous-Material Model for Sand with Different Levels of Water Saturation, *Soil Dyn. Earthq. Eng.*, 2008, **28**, p 20–35
22. M. Grujicic, B. Pandurangan, U. Zecevic, K.L. Koudela, and B.A. Cheeseman, Ballistic Performance of Alumina/S-2 Glass-Reinforced Polymer-Matrix Composite Hybrid Lightweight Armor Against Armor Piercing (AP) and Non-AP Projectiles, *Multidiscip. Model. Mater. Struct.*, 2007, **3**, p 287–312